Acta Materialia 204 (2021) 116514

Contents lists available at ScienceDirect

Acta Materialia

journal homepage: www.elsevier.com/locate/actamat

Full length article

Accommodation and formation of $\{\bar{1}012\}$ twins in Mg-Y alloys

Krishna Yaddanapudi[a,*], Brandon Leu[b], M. Arul Kumar[c], Xin Wang[d], Julie M. Schoenung[d], Enrique J. Lavernia[d], Timothy J. Rupert[d], Irene J. Beyerlein[b], Subhash Mahajan[a]

[a] Department of Materials Science and Engineering, University of California, Davis, CA 95616, USA
[b] Department of Mechanical Engineering, Materials Department, University of California, Santa Barbara, CA 93106, USA
[c] Materials Science and Technology Division, Los Alamos National Laboratory, Los Alamos, NM 87545, USA
[d] Department of Materials Science and Engineering, University of California, Irvine, CA 92697, USA

ARTICLE INFO

Article history:
Received 23 August 2020
Revised 1 November 2020
Accepted 20 November 2020
Available online 30 November 2020

Keywords:
Magnesium alloys
Deformation twinning
Emissary slip
Transmission electron microscopy
Crystal plasticity

ABSTRACT

The $\{\bar{1}012\}$ tensile twins terminating inside the grains of a deformed Mg-Y alloy were investigated by transmission electron microscopy. The crystallographic features of terminating twins and associated slip structures were quantified and correlated. The local stresses developed at a terminating $\{\bar{1}012\}$ twin were computed using crystal plasticity simulations in order to interpret the observed slip patterns. Results indicate that both basal $\langle a\rangle$ and $\langle c+a\rangle$ matrix glide were involved in accommodating the plastic stresses developed in the vicinity of terminating twins. Along the twin boundary, the defect contrast consistent with that of lattice dislocations and twinning partials was observed. Based on these observations, a dislocation reaction is proposed that establishes an interrelationship between the observed matrix glide and $\{\bar{1}012\}$ twinning in Mg-Y alloys.

1. Introduction

Hexagonal close packed (hcp) magnesium and its alloys are one of the most desirable candidates for structural applications, where specific strength and weight are decisive factors for reducing the energy consumption [1,2]. Therefore, understanding the mechanisms that govern the strength of Mg alloys is becoming increasingly important. When mechanically strained, these alloys deform permanently by slip and twinning. A question of fundamental importance is how these two mechanisms are interrelated.

The most widely observed twinning mode in Mg alloys is the $\frac{1}{15}\langle\bar{1}01\bar{1}\rangle\{\bar{1}012\}$ twin, which accommodates tensile strain along the $\langle c\rangle$-axis [3–5]. This type of tensile twin can develop readily compared to other twinning modes [4], and they can terminate at grain boundaries, inside the grains, or at other twins. They often appear as high aspect ratio lamellae and often with thickness much finer than the grain size. Very high stresses are developed in the immediate vicinity of terminating twins, and if they are not relaxed plastically, could nucleate cracks or voids [6–9]. Earlier studies showed that stresses which develop at $\frac{1}{6}\langle111\rangle\{11\bar{2}\}$ and $\frac{1}{6}\langle11\bar{2}\rangle\{111\}$ deformation twins terminating inside the matrix of body centered cubic (bcc) and face centered cubic (fcc) metals, are plastically relaxed by slip occurring in the matrix regions just ahead of twins [10–12]. This relaxation mechanism was explained by the phenomenon of *emissary slip*, where twinning partials bounding a twin tip could interact and generate matrix glide to accommodate plastic stresses developed in the vicinity of terminating twins [13]. In bcc and fcc crystals, the phenomenon of emissary slip was well explained by the following reactions [10,11].

$$3\times\frac{1}{6}\langle111\rangle_{\{11\bar{2}\}}\rightarrow\frac{1}{2}\langle111\rangle_{\{11\bar{2}\}}\qquad\text{(bcc)}\qquad(1)$$

$$3\times\frac{1}{6}\langle11\bar{2}\rangle_{\{111\}}\rightarrow\frac{1}{2}\langle01\bar{1}\rangle_{\{111\}}+\frac{1}{2}\langle10\bar{1}\rangle_{\{111\}}\qquad\text{(fcc)}\qquad(2)$$

According to these reactions, for instance, three $\frac{1}{6}\langle111\rangle$ twinning partials present on adjacent $\{11\bar{2}\}$ twin planes may interact and coalesce into $\frac{1}{2}\langle111\rangle$ matrix dislocations in bcc crystals. The glide of these matrix dislocations on $\{11\bar{2}\}$ planes could relax the plastic stresses developed ahead of twins. A similar explanation can be obtained for equation (2) in fcc crystals. In a later study, Vaidya and Mahajan [14] proposed an interrelationship between $\frac{1}{36}\langle\bar{1}\bar{1}26\rangle\{11\bar{2}1\}$ twinning and slip in hcp Co crystals, which is totally consistent with the theory of emissary slip. The authors showed that glissile $\langle c+a\rangle$ and $\langle1\bar{1}00\rangle$ matrix glide were involved in accommodating the plastic stresses developed ahead of $\{11\bar{2}1\}$ twins and twin-twin intersections in hcp Co [14].

To date, similar investigations on the relaxation of plastic stresses developed at $\{\bar{1}012\}$ terminating twins in hcp Mg alloys have not been carried out. A few investigations are available that

* Corresponding author. fax: 5302207075.
E-mail address: grkyaddanapudi@ucdavis.edu (K. Yaddanapudi).

https://doi.org/10.1016/j.actamat.2020.116514

focus on the accommodation of tensile twins in Mg alloys [7,15–17]. Based on optical microscopy studies, Roberts et al. [15] reported accommodation by kinking adjacent to terminating tensile twins in pure Mg. Using electron back scattered diffraction (EBSD) and simulations, Jonas et al. [16] proposed that in the accommodation zone close to the tensile twin, local strains are accommodated by $\langle c+a \rangle$ matrix glide or additional mechanical twinning. With finite element modeling, Barnett et al. [7] showed that the back stress induced by a tensile twin in AZ31 Mg alloys is relaxed by the glide of matrix dislocations. As a validation, high-resolution EBSD studies revealed higher activity of $\langle a \rangle$ and $\langle c+a \rangle$ dislocations in the matrix regions surrounding the tensile twin tips [17]. While prior microstructural based observations were valuable, a systematic interrelationship between $\{\bar{1}012\}$ twinning shear and matrix glide, which is consistent with the theory of emissary slip and hence the accommodation process of $\{\bar{1}012\}$ twins in Mg alloys has yet to be pursued.

The objective of this paper is to understand the accommodation of plastic stresses developed at $\{\bar{1}012\}$ twins that have stopped propagating inside the grains. Meeting this goal entails investigating the interrelationship between all matrix dislocations, e.g., basal $\langle a \rangle$, prismatic $\langle a \rangle$ and pyramidal $\langle c+a \rangle$, and tensile twins and a model Mg alloy that can activate all three slip modes and is prone to tensile twinning. The activation of pyramidal $\langle c+a \rangle$ slip in most Mg alloys is limited. Extensive literature suggests that addition of Li and Y enhances $\langle c+a \rangle$ slip activity and thus, improves the ductility of Mg [18–21]. For these reasons, we elect to examine a single phase Mg alloy containing 0.6 wt.% Y as a model material system.

The crystallographic features of terminating twins and associated dislocation structures formed in the deformed Mg-0.6 wt.% Y alloy were examined and correlated by TEM. Based on TEM observations and with the help of discrete three-dimensional (3D) twin calculations based on crystal plasticity, a dislocation reaction is proposed that establishes an interrelationship between slip and $\{\bar{1}012\}$ twinning in Mg-Y alloys.

2. Experimental methods

Mg-0.6 wt.% Y alloys were obtained from the Helmholtz-Zentrum Geesthacht Centre for Materials and Coastal Research. The homogenization of cast ingots and hot rolling were performed at a temperature of 500 °C. Subsequent annealing was performed at a temperature of 400 °C for 10 min. The annealed alloy had an average grain size of $21\mu m$, as measured using the optical microscopy. The annealed rolled sheet was sectioned using electrical discharge machining (EDM) to make cuboids of dimensions $3.3\,mm \times 3.3\,mm \times 5mm$. The cuboids were then deformed in compression at ambient temperature to an engineering strain of approximately 1.2% along the normal direction (ND). The microstructure of the deformed alloy was examined using JEOL JEM 2100F-AC TEM, operating at 200 kV. TEM samples were prepared using FEI Scios dual-beam focused ion beam (FIB) equipped with a gallium-ion source. Easy-lift needle manipulator was used to lift, transfer and attach the samples to Cu grids. To prevent beam induced damage the subsequent thinning of the lamella was done at low accelerating voltages ranging from 12 kV to 1 kV, and at low ion-beam currents ranging from 1 nA to 20 pA. The prepared TEM lamella and their crystallographic orientations in relation to the macroscopic sample directions are described in section S1 of the supplementary material (SM).

The crystallography of $\{\bar{1}012\}$ terminating twins such as the orientation and habit plane, was studied from the selected area electron diffraction (SAED) patterns. The Burgers vectors of the matrix dislocations were determined using the invisibility criteria, where a perfect lattice dislocation becomes invisible or exhibits weak residual contrast when the product $\mathbf{g}\cdot\mathbf{b}=0$, where $\mathbf{g}$ is the operating reflection vector used and $\mathbf{b}$ is the corresponding Burgers vector of the dislocation. The glide (habit) planes of dislocations (twins) were identified from the diffraction analysis coupled with the surface trace analysis.

3. Results

To establish interrelationship between slip and $\{\bar{1}012\}$ twinning shear in Mg-0.6 wt.% Y alloys, two different cases were considered. In the first case, dislocation structures in a deformed twin-free grain were studied. This grain is labeled as grain-2 in this study. In the second case, the crystallographic features of $\{\bar{1}012\}$ twins terminating inside the deformed grains and associated slip structures were investigated in detail. The corresponding grains are labeled as grain-1 and grain-3. In addition, crystal plasticity calculations of a 3D terminating $\{\bar{1}012\}$ twin tip were performed in order to correlate the local stresses developed around the twin tip with the slip activity they induce. The following sections describe the results obtained from these investigations.

3.1. Dislocation structures in a deformed twin-free grain

The twin-free grain (i.e. grain-2) was deformed in compression along the $[0\bar{1}13]$ direction, which is parallel to the macroscopic sample ND in this study. The TD is found to parallel to the $[\bar{1}5\bar{4}3]$ direction of grain-2 as described in Figure S2 of the SM. The possible slip and twin systems that exhibit maximum Schmid factor values for this grain and for the deformation conditions used in this work have been tabulated in Table S5.2 of the SM.

Fig. 1 (a) shows the microstructure of this grain, and it consists of slip dislocations and an intragranular sub-boundary associated with an array of dislocations. The TEM investigations confirm that these dislocations are $\langle c+a \rangle$ in nature. No $\langle a \rangle$ and $\langle c \rangle$ dislocations were observed. The Burgers vector analysis for these $\langle c+a \rangle$ dislocations is described in Figs. 1(b)-1(f) for various operating reflections. The black arrows pointing three dislocations on the micrographs are to indicate the variation in dislocation contrast for the reflection conditions used in this analysis.

From Figs. 1(b) and 1(d), it is clear that dislocations that are visible for the operating reflection $g=0002$ are invisible for the reflection $g=10\bar{1}\bar{1}$, suggesting that the dislocations are $\langle c+a \rangle$ in nature. The dislocation contrast analysis for the operating reflections $g=0002$, $10\bar{1}0$, $10\bar{1}\bar{1}$, $10\bar{1}1$, and $\bar{1}100$ in Figs. 1(b)-1(f), confirms $\frac{1}{3}[2\bar{1}\bar{1}3]$ as the Burgers vector for these $\langle c+a \rangle$ dislocations. The possible Burgers vectors of dislocations available for the operating reflections used in this analysis are tabulated in Table S2.1 of the SM.

Single-surface trace analysis in combination with the diffraction analysis shows that the projections of these $\langle c+a \rangle$ dislocations are parallel to the trace of $(\bar{1}011)$ plane as indicated by the white colored dashed line in Fig. 1(b). Tilting the sample to a high index zone axis (i.e., $[\bar{2}7\bar{5}3]$, in Figs. 2(a) and 2(b)), and carrying out subsequent trace analysis further confirms $(\bar{1}011)$ as the glide plane for the $\langle c+a \rangle$ dislocations. Fig. 2(b) shows a weak-beam dark-field (**g/3g**) image of the same $\langle c+a \rangle$ dislocations present along the sub-boundary with their projected line segments parallel to the trace of $(\bar{1}011)$ plane. A careful examination of Fig. 2(b) also reveals the signature of Moiré fringes on either side of the dislocation array, which could often visible as a result of deformation induced rotation of matrix regions. The grain-2, thus, consists of glissile $\langle c+a \rangle$ dislocations belonging to the slip system, $\frac{1}{3}[2\bar{1}\bar{1}3](\bar{1}011)$. The corresponding Schmid factor value for this slip system is found to be 0.45 for the deformation conditions used in this work (see Table S5.2 of the SM).

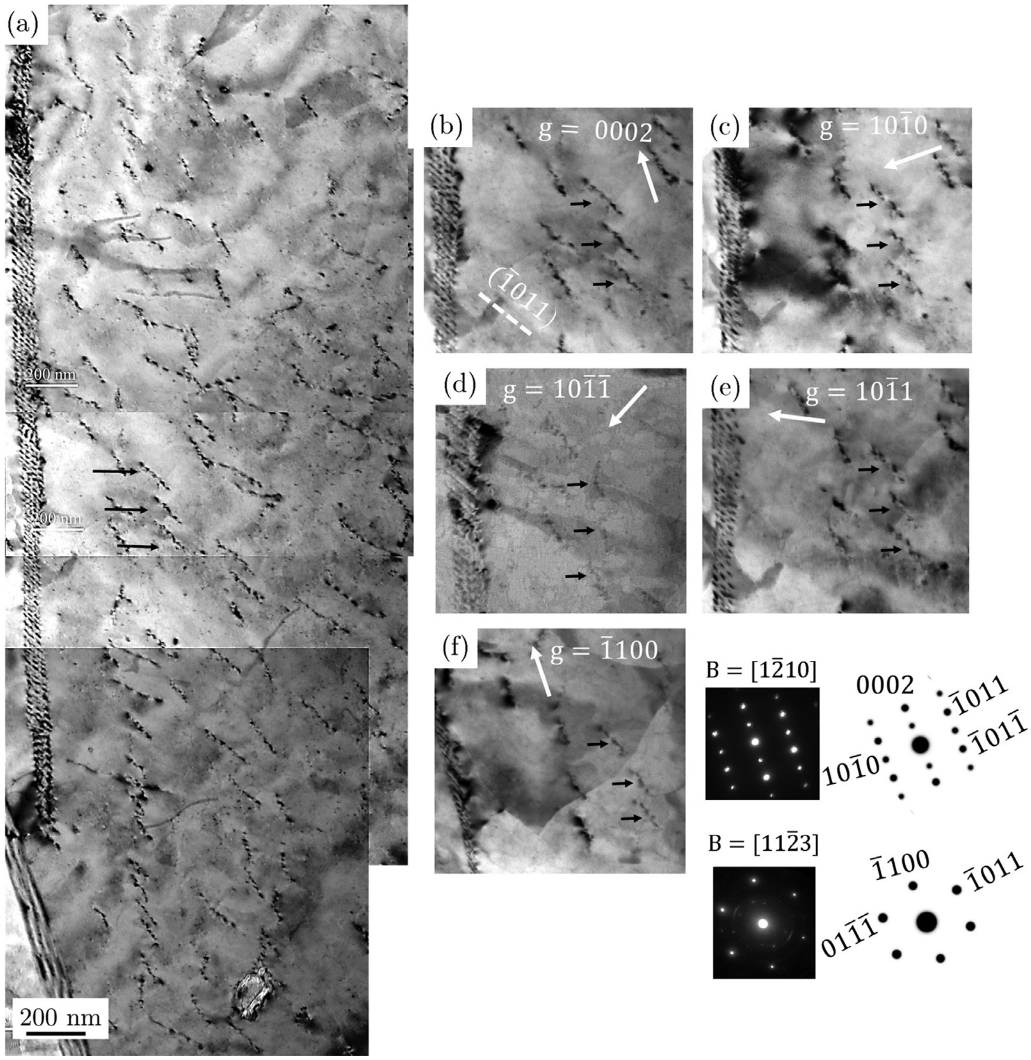

Fig. 1. A bright field TEM micrograph of the deformed microstructure obtained from a twin-free grain (i.e. grain-2). The microstructure consists of slip dislocations and an intragranular sub-boundary associated with an array of dislocations (a). The images (b)-(f) were acquired under two-beam bright field diffracting conditions using various operating reflections as mentioned on each micrograph, and for the $[1\bar{2}10]$ and $[11\bar{2}3]$ orientations of grain-2. The corresponding SAED patterns are also provided in the image along with the simulated patterns. The black colored arrows pointing three dislocations indicate the variation in dislocation contrast for different operating reflections. The white colored dashed line represents the traces of $(\bar{1}011)$ pyramidal-I plane, which is in an egde-on orientation (b).

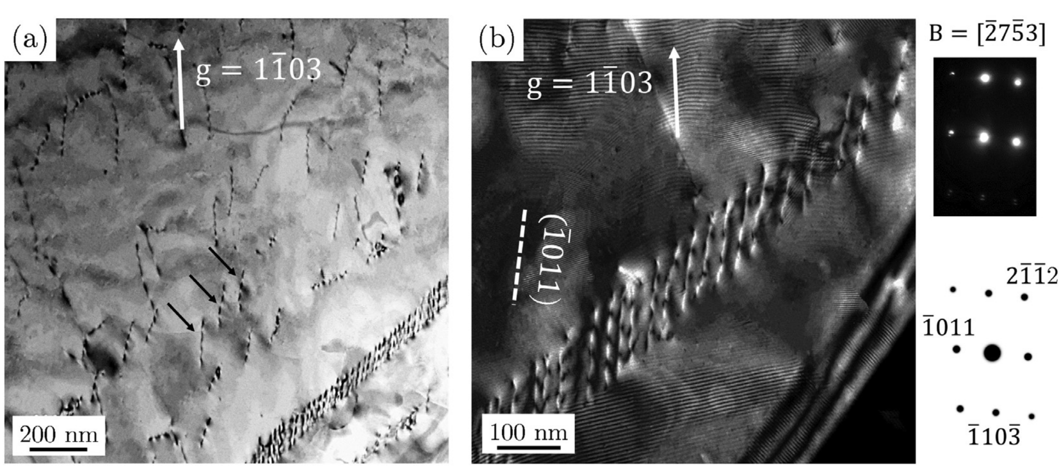

Fig. 2. TEM images of the same glissile pyramidal-I $\langle c+a \rangle$ slip dislocations shown in Fig. 1, however, for the $[\bar{2}7\bar{5}3]$ orientation and for $g = 1\bar{1}03$ reflection of the matrix (a). Weak beam dark field image of the intragranular sub-boundary showing the projections of dislocations parallel to the trace of $(\bar{1}011)$ pyramidal-I plane (b).

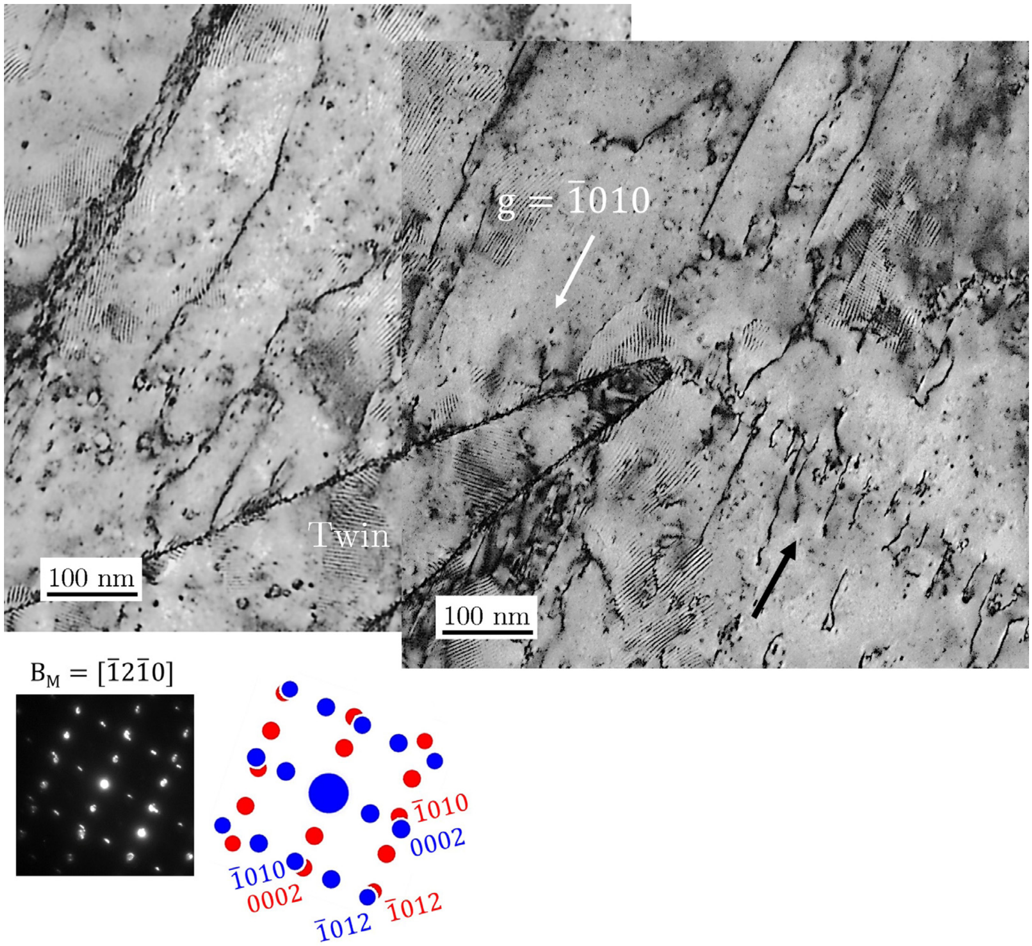

Fig. 3. (a) TEM image of a tensile twin terminating inside the grain-1 of deformed alloy. The grain-1 is oriented along the $[\bar{1}2\bar{1}0]$ direction. The experimental SAED pattern is provided along with the simulated pattern, where blue colored spots represent the matrix and red colored spots represent twin. The black colored arrow on the plane of the micrograph represents a dislocation array, which appears to be connected with the twin tip. (For interpretation of the references to colour in this figure legend, the reader is referred to the web version of this article.)

3.2. Crystallography of a terminating twin

Fig. 3 shows a twin that has terminated inside the grain-1 of the deformed Mg-0.6 wt.% Y alloy. This grain was deformed in compression along the $[\bar{1}010]$ direction, which is the macroscopic sample ND as shown in Figure S2 of the SM. The possible slip and tensile twin systems that exhibit maximum Schmid factor values for this grain have been tabulated in Table S5.1 of the SM.

The experimental SAED pattern acquired from this region is shown in Fig. 3, for the $[\bar{1}2\bar{1}0]$ orientation of grain-1. The corresponding crystallographic orientation of twin (i.e.$[1\bar{2}10]$) was obtained using the twinning transformation matrices derived by Niewczas [22]. The SAED pattern consists of spots corresponding to matrix as well as the twin. These spots were indexed carefully and are represented by red (twin) and blue (matrix) colored spots in the simulated pattern. The diffraction and surface trace analysis confirms that the twin is a tensile twin with $(\bar{1}012)$ as the habit plane. The Schmid factor analysis shows a maximum value of 0.49 for the twin system $(\bar{1}012)[\bar{1}01\bar{1}]$ (see Table S5.1 in the SM).

3.3. Slip activity in the vicinity of twin tip

Fig. 3 shows significant dislocation activity in matrix regions surrounding the twin. First, a dislocation array that appears to be connected to the twin tip (indicated by a black arrow) is observed. TEM investigations revealed that this dislocation array predominantly consists of $\langle c+a \rangle$ dislocations and a few $\langle a \rangle$ dislocations. The remaining long projected line segments seen in the vicinity of twin tip are found to be $\langle a \rangle$-type in this study. Fig. 4 describes the Burgers vector analysis of these dislocations for various operating reflections.

Figs. 4 (a) to 4(d) show that the dislocation contrast that is visible (indicated by short white arrows) for the reflections $g = \bar{1}010, 10\bar{1}1$, and $01\bar{1}\bar{1}$ is invisible for the reflection $g = 0002$ in Fig. 4(a). This result confirms that the contrast must be due to $< a >$-type dislocations having the Burgers vector: $\mathbf{b} = \frac{1}{3}[\bar{1}\bar{1}20]$. The projected line segments of these dislocations are nearly parallel to the trace of basal plane of the matrix, which is in an edge-on orientation for the $[\bar{1}2\bar{1}0]$ orientation of the matrix. The TEM investigations, thus, confirm that $\langle a \rangle$ dislocations seen in Fig. 4, belong to the $\frac{1}{3}[\bar{1}\bar{1}20](0001)$ slip system. The long straight dislocations shown in the surroundings of the twin tip in Fig. 3, also found to satisfy the above reflection conditions and thus, exhibit the same Burgers vector.

The contrast from the dislocations indicated by the black arrow, i.e., the dislocation array in Fig. 4, is visible for all the four operating reflections $g = \bar{1}010, 10\bar{1}1, 01\bar{1}\bar{1}$, and 0002, suggesting that these dislocations are $\langle c+a \rangle$ in nature and satisfy the following Burgers vector: $\mathbf{b} = \frac{1}{3}[\bar{2}11\bar{3}]$. Careful examination reveals the zigzag nature of these dislocations. The magnified view (enclosed by blue boxes) of dislocations shown in Fig. 4(a) for $g = 0002$ reflection indicates that the projections are nearly parallel to the trace of

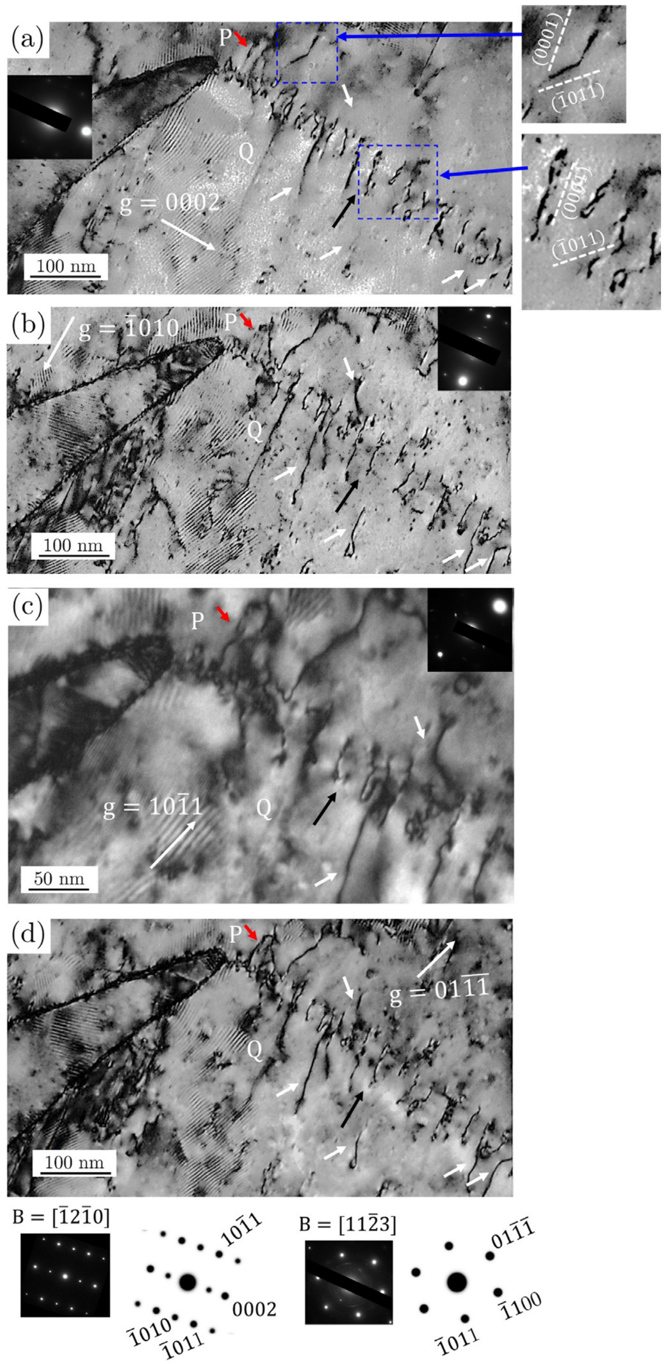

Fig. 4. Two-beam bright-field TEM images of $(\bar{1}012)$ tensile twin terminating inside the grain-1 of the deformed alloy. The images were acquired under (a), (b), (c) $[\bar{1}2\bar{1}0]$, and (d) $[11\bar{2}3]$ orientations of grain-1, and using various operating reflections. The corresponding SAED patterns are also provided along with the simulated patterns. The white colored dashed lines represent the traces of the basal and $(\bar{1}011)$ pyramidal-I planes (a). The short white colored arrows indicate the basal $\langle a\rangle$ dislocations in the array, while rest of the dislocations in the array are found to be $\langle c+a\rangle$ (indicated by a black arrow).

$(\bar{1}011)$ pyramidal-I plane and the basal plane. Both of these planes are in an edge-on orientation for the $[\bar{1}2\bar{1}0]$ orientation of the matrix (see the SAED pattern).

The contrast of $\langle c+a\rangle$ dislocations parallel to the basal plane was reported in Mg alloys [18,23,24]. It was suggested that $\langle c+a\rangle$ dislocations could glide on pyramidal planes and blocked at the line of intersection with the basal plane, resulting in a dislocation contrast parallel to the trace of the basal plane [18,23,24]. For the orientation of matrix in Fig. 4, it is difficult to find those pyramidal planes which contribute the contrast parallel to the basal plane. Nevertheless, for the Burgers vector $\frac{1}{3}[\bar{2}11\bar{3}]$, it is geometrically possible the glide of $\langle c+a\rangle$ dislocations on $(\bar{1}101)$ and $(\bar{2}112)$ planes, which are not in an edge-on orientation in Fig. 4. The $\langle c+a\rangle$ dislocations blocked at the line of intersection of these planes with the basal plane could yield contrast parallel to the basal plane. Figure S3 in the SM geometrically shows these two pyramidal planes along with the $(\bar{1}011)$ plane and their line of intersections with the basal plane. Taken together, the TEM investigations confirm that the $\langle c+a\rangle$ slip dislocations seen in the array have the Burgers vector $\frac{1}{3}[\bar{2}11\bar{3}]$ with line contrast parallel to the trace of basal and $(\bar{1}011)$ pyramidal-I planes. The zig-zag nature observed may be a result of cross-slip of $\langle c+a\rangle$ dislocations on the pyramidal planes. The Schmid factor analysis yields a maximum of 0.4 value for the $\frac{1}{3}[\bar{2}11\bar{3}](\bar{1}011)$ slip system and for the deformation conditions used in this work (see Table S5.1 of the SM). The possible Burgers vectors of dislocations available for the operating reflections used in this analysis are tabulated in Table S2.2 of the SM.

Unlike the $\langle a\rangle$ and $\langle c+a\rangle$ dislocations described above, the dislocation marked 'P' in Fig. 4 (red arrow), exhibits a different Burgers vector. It is invisible for the operating reflection $g=\bar{1}010$, and exhibits a contrast for the reflections $g=0002$, $10\bar{1}1$ and $01\bar{1}\bar{1}$, indicating that the dislocation must be $\langle c+a\rangle$ in nature and satisfy the $\mathbf{b}=\frac{1}{3}[\bar{1}2\bar{1}\bar{3}]$ Burgers vector. However, the Burgers vector of the dislocation labeled 'Q' in Fig. 4, is not well understood for the operating reflections used in this study. The TEM investigations, thus, confirm that the dislocation array associated with the terminating twin tip in grain-1 consists of two sets of dislocations, i.e., $\langle a\rangle$ and $\langle c+a\rangle$ dislocations. The different Burgers vectors of these dislocations suggest that the array is not formed as a result of dislocation pile-up, for instance, from a sub-grain boundary. A careful examination of Figs. 3 and 4 for various operating reflections also reveals the signature of Moiré fringes in the matrix as well as in the twin domain, which could often originate as a result of deformation induced rotation of the Mg lattice.

3.4. Diffraction contrast along the twin boundary

Fig. 5 shows the magnified images of the same twin tip, which is described in Fig. 4. Careful examination of $(\bar{1}012)$ twin boundary in Fig. 5 for various operating reflections, reveals changes in diffraction contrast along the twin boundary, which could be signs of twinning partials and other crystallographic defects. To identify the character of these defects, we employ the $\mathbf{g}\cdot\mathbf{b}$ invisibility criteria using the same operating reflections described in Fig. 4.

It is clear that the dark contrast that is present along the twin boundary for $g=\bar{1}010$ reflection in Fig. 5(a), is invisible at some specific locations in Fig. 5(b) (indicated by small white arrows) for the operating reflection $g=0002$. This result indicates that the defects that satisfies this extinction condition must have $\langle a\rangle$ component. They likely result from their interactions with the twin boundary during deformation. The same locations were indicated by small white arrows in Fig. 5(c) and 5(d) for the reflections $g=10\bar{1}1$ and $01\bar{1}\bar{1}$. The invisibility criteria for these four operating reflections, therefore, identifies $\mathbf{b}=\frac{1}{3}[\bar{1}\bar{1}20]$ as the Burgers vector for these $\langle a\rangle$ dislocations.

The dark contrast regions along the twin boundary in Fig. 5(b) (black arrows) for the reflection $g=0002$ results either from the defects having $\langle c+a\rangle$ component or from the twinning partials. The same locations are indicated by black arrows in Fig. 5(a), 5(c) and 5(d) for the operating reflections $g=\bar{1}010$, $10\bar{1}1$, and $01\bar{1}\bar{1}$. Assuming those defects are $\langle c+a\rangle$ dislocations, the analysis iden-

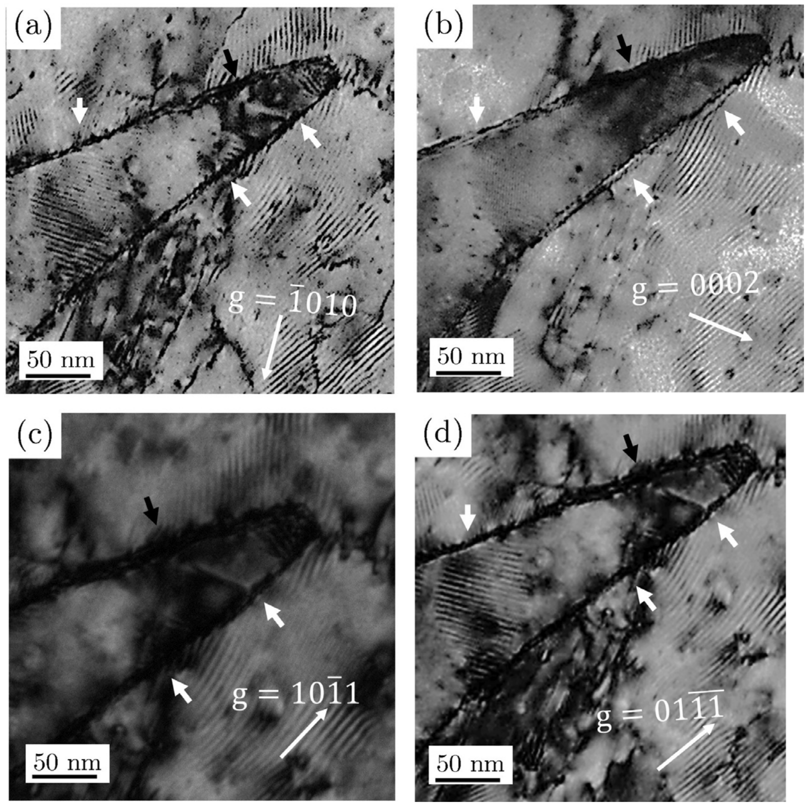

Fig. 5. Magnified view of the tensile twin tip which has terminated inside grain-1. The images were obtained under two different zone axes: (a), (b), (c) $[\bar{1}2\bar{1}0]$ and (d) $[11\bar{2}3]$ and for various operating reflections as described in Fig. 4. The black and white colored short arrows point the changes in diffraction contrast at some specific regions along the twin boundary, and for the operating reflections displayed on the micrographs.

Table 1
The $\mathbf{g} \cdot \mathbf{b}$ values for the observed lattice dislocations and twinning partials for the operating reflections used in this study.

$\mathbf{g} \cdot \mathbf{b}$	$\pm\frac{1}{3}[\bar{1}\bar{1}20]$	$\pm\frac{1}{3}[\bar{2}11\bar{3}]$	$15 \times \{\pm\frac{1}{15}[\bar{1}01\bar{1}]\}$
0002	0	∓ 2	∓ 2
$\bar{1}010$	∓ 1	∓ 1	∓ 2
$10\bar{1}1$	∓ 1	∓ 2	∓ 3
$01\bar{1}\bar{1}$	∓ 1	± 1	0

tifies the Burgers vector of these dislocations to be $\mathbf{b} = \frac{1}{3}[\bar{2}11\bar{3}]$. It should be noted that the obtained Burgers vectors of $\langle a \rangle$ and $\langle c + a \rangle$ dislocations are same as those observed in the dislocation array described in Section 3.3.

The Burgers vector of twinning partials for $(\bar{1}012)$ twin is: $\mathbf{b}_{tw} = \frac{1}{15}[\bar{1}01\bar{1}]$ [25], which is too small to produce significant diffraction contrast. However, a collection of twinning partials can produce significant diffraction contrast along the twin boundary. For instance, a group of 15 twinning partials can yield $\mathbf{g} \cdot \mathbf{b}_{tw}$ values comparable to that of lattice dislocations as mentioned in Table 1. The invisibility criteria analysis indicates that the defect contrast observed along the twin boundary in Figs. 5(a)-5(c) is also consistent with that of twinning partials having the Burgers vector $\mathbf{b}_{tw} = \frac{1}{15}[\bar{1}01\bar{1}]$. However, it should be noted that the four reflections in Table 1 are not sufficient to distinguish the diffraction contrast originating from the lattice dislocations and twinning partials, and it requires a further study. In summary, the TEM investigations confirm that the defect contrast along the twin boundary is attributed to $\langle a \rangle$ and $\langle c + a \rangle$ matrix dislocations having Burgers vector inclined to the co-zone axis, as well as to the twinning partials of the $(\bar{1}012)$ twin.

3.5. Crystal plasticity calculations for a terminating twin

To relate the local stresses induced by the terminating tensile twins and the dislocations observed in the foregoing TEM analysis, a full-field elasto-visco-plastic Fast Fourier Transform (EVP-FFT) model was employed. The original EVP-FFT model treated both elastic and viscoplastic effects in heterostructured polycrystals and has been advanced to include discrete twin lamellae within crystals [26,27]. The model simulates twinning deformation by reorienting and shearing a predefined twin region within a crystal. The reorientation is defined by its crystallographic relationship with the parent crystal and shear is determined by the characteristic shear of the twin type. Imposing the latter can generate severe plastic strains locally in the surrounding crystal and therefore, within the twin region the total twin shear is achieved by incrementally shearing along the twin plane in the twinning shear direction over several steps (e.g., two thousand). After each increment, the simulation cell is energetically relaxed and the stresses and strains at each Fourier point are updated. Once the appropriate twinning transformation and eigenstrain are accomplished, the twin is considered fully developed. The FFT formulation employs periodic unit cells and provides an exact solution to the governing equations of equilibrium, compatibility, and standard constitutive relationships at each discrete Fourier point, bounded by the user defined limitations and discretization of the numerical algorithm. The local stresses and strains at each Fourier point are related by the following discretized constitutive law:

$$\boldsymbol{\sigma}^{t+\Delta t}(X) = \mathbf{C}(X) : (\epsilon^{t+\Delta t}(X) - \epsilon^{p,t}(X) - \dot{\epsilon}^{p,t+\Delta t}(X, \boldsymbol{\sigma}^{t+\Delta t})\Delta t) \quad (3)$$

In the above equation, at each material point X, $\boldsymbol{\sigma}(X)$ is the Cauchy stress tensor, $\mathbf{C}(X)$ is the elastic stiffness tensor, and

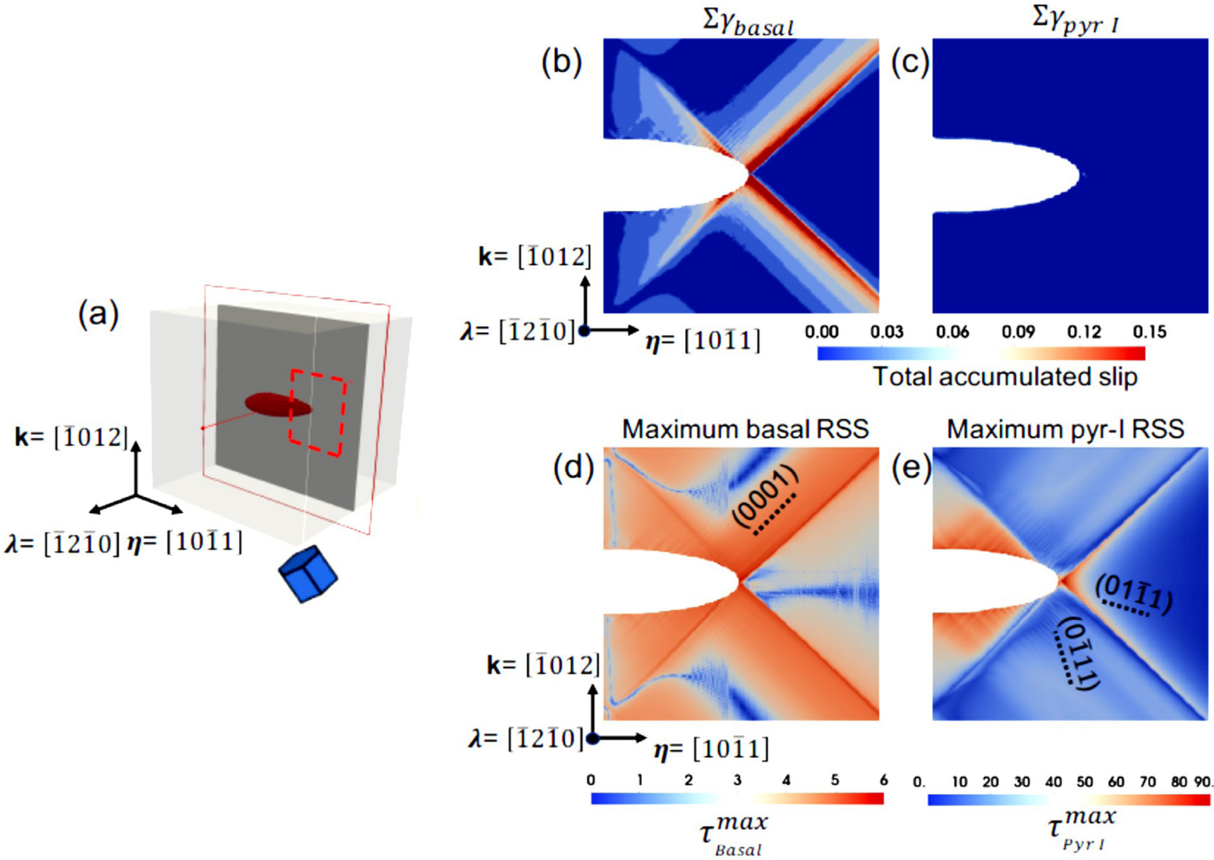

Fig. 6. 2D representation of the simulation cell containing a fully developed twin (red) embedded in a Mg-Y parent matrix (gray). The orientation axes and the hexagonal inset represent the orientation of the parent matrix. (a) Schematic representing the formation of a twin in the interior of a Mg parent grain. The solid red box outlines the plane of interest that is used for the 2D simulation. The dashed red box highlights the region at the twin tip used for analysis. (b) and (c) show the total accumulated slip among the basal and pyramidal-I slip modes, respectively, that result of forming the twin. (d) and (e) show the maximum RSS among basal and pyramidal-I slip modes, respectively, from the formation of the twin. The dashed lines illustrate the slip plane traces of the slip systems with the highest RSS. (For interpretation of the references to colour in this figure legend, the reader is referred to the web version of this article.)

$\epsilon(X), \epsilon^p(X), \dot{\epsilon}^p(X)$ correspond to the total strain, plastic strain, and plastic strain rate, respectively. Within each point of the twin domain, the lattice is reoriented and a twinning shear transformation is incrementally imposed following:

$$\Delta\epsilon^{twin}(X) = \mathbf{m}^{twin}(X)\Delta\boldsymbol{\gamma}^{twin}(X). \quad (4)$$

The tensor $\mathbf{m}$ is the Schmid tensor associated with the twin system and the incremental twin shear $\Delta\boldsymbol{\gamma}^{twin}(X)$ is the characteristic twinning shear divided by N increments to ensure convergence.

Fig. 6 (a) shows the periodic cell of the twin model, which consists of a 3D ellipsoidal twin embedded in a matrix of Mg-Y. The twin is thick in the center and comes to a point on the twin plane. The crystallographic orientation of the parent matrix is assigned to be $(0^o, 45^o, 0^o)$ in the Bunge convention, which aligns the twin shear direction, $\boldsymbol{\eta}$, twin plane normal, $\mathbf{k}$, and lateral direction, $\boldsymbol{\lambda}$, with the edges of the unit cell. The hexagonal inset shows the orientation of the parent crystal. Surrounding the parent matrix, is a layer of polycrystalline Mg with a random texture, which is not shown in the figure. The matrix and twin crystals are discretized into $150 \times 150 \times 150$ voxels. The outer polycrystalline layer is 24 voxels thick in each direction, a thickness found to be sufficiently to minimize any effects, such as overlapping fields, of periodic boundary conditions. From this 3D cell, a planar slice of the original simulation cell is shown in Fig. 6(a). The thin twin model is meant to represent the cross-section analyzed in the TEM foil. While the buffer layer remains in 24-voxels thick, the discretization of the matrix and twin crystals is increased to $3 \times 500 \times 500$ and no buffer layer was used in the out-of-plane direction. The in-plane coordinates of the 2D slice mirror the $[\bar{1}2\bar{1}0]$ zone-axis conditions described in Fig. 3.

The prismatic, basal and pyramidal-I slip modes are made available in the calculation for plastic deformation. In a separate work [28], the critical resolved shear stresses (CRSS) were characterized via polycrystal modeling. Tension or compression responses for the same alloy were measured along three orientations and the texture evolution and twinning activity were studied. A single set of CRSS values of 45, 5, and 86 MPa, for prismatic, basal and pyramidal-I slip, respectively, were identified [28], and these same values are used here.

Calculations of the mechanical fields everywhere in the 3D bulk model and planar slice model are performed and generally the fields are similar to first order. The former simulation best represents the fields in bulk, while the slice model best represents those seen in the TEM analysis and thus, in the interest of space, the 3D simulation are shown in section S6 of the SM, while the slice model results are shown in Fig. 6. In both simulations, no external load was applied before the formation of the twin in order to better isolate the stress fields that develop from the twinning process.

Fig. 6 shows the spatial distribution of total accumulated basal slip and pyramidal-I slip ahead of the twin. In equation (3), the plastic strain rate is the net contribution to plastic strain by the shear rates along individual crystallographic slip systems, and is calculated using

$$\dot{\epsilon}^{p}(X) = \sum_{s=1}^{N} \mathbf{m}^{s}(X)\dot{\gamma}^{s}(X) = \dot{\gamma}_0 \sum_{s=1}^{N} \mathbf{m}^{s}(X)\left(\frac{|\mathbf{m}^{s}(X):\boldsymbol{\sigma}(X)|}{\tau_0^{s}}\right) sgn(\mathbf{m}^{s}(X):\boldsymbol{\sigma}(X)) \quad (5)$$

where tensor $\boldsymbol{s}$ is the Schmid tensor associated with the slip system s, τ_0^s is the CRSS, and $\dot{\gamma}_0$ is a nominal strain rate, commonly assigned the applied strain rate. The total accumulated basal slip is the sum of the shear rates $\dot{\boldsymbol{\gamma}}^{s}(X)$ on all basal slip systems multiplied by the simulation time increment. Similarly, for the accumulated pyramidal-I slip, it corresponds to the sum of the shear rates of all pyramidal-I slip systems multiplied by the simulation time increment. Large amounts of basal slip accumulated, particularly in thin ribbons lying diagonally from the twin tip. These regions are consistent with the locations of the $\langle a\rangle$ dislocations observed around the twin tip in Fig. 3. The calculations indicate that no pyramidal slip accumulated in the region ahead of the twin tip (Fig. 6(c)). Distributions of prismatic slip are, however, not shown since prismatic slip was not predicted. Therefore, the twin shear is accommodated predominantly by basal slip.

To evaluate the instantaneous driving forces and the most active slip system, we plot in Figs. 6(d) and 6(e) the spatial distribution of the highest resolved shear stresses (RSS) among all basal $\langle a\rangle$ and pyramidal-I $\langle c+a\rangle$ slip systems, respectively. The RSS fields in the twinned region are omitted for visualization. The traces of basal and pyramidal-I slip systems with the highest RSS are indicated with dashed lines. The calculations reveal that active basal and pyramidal slip concentrate in specific regions surrounding the twin. The maximum basal RSS slip system is $[11\bar{2}0](0001)$ and is intense only at the leading edge of the twin tip in the $[10\bar{1}1]$ direction and within narrow regions emanating from the twin tip. However, immediately adjacent to these regions and ahead of the twin tip, it is nearly zero. These high RSS basal regions and the basal slip system with the highest RSS agree are similar to the locations of basal dislocations seen in the TEM analysis. As shown in Fig. 6(e), intense fields of pyramidal RSS (in the $[10\bar{1}1]$ direction) concentrate strongly at twin tip and within thin ribbons radiating diagonally from the twin tip, which is consistent with the location of $\langle c+a\rangle$ dislocation array seen in TEM. High pyramidal-I RSS also develops along the twin boundary. The maximum RSS slip system is $\frac{1}{3}[\bar{2}11\bar{3}](\bar{1}011)$, the same as the one belonging to the $\langle c+a\rangle$ dislocation array seen in TEM and the slip system traces align well with the observed $\langle c+a\rangle$ dislocation array in Fig. 3. Considering both the accumulated slip and max RSS fields suggests that pyramidal-I slip does not occur within broad regions around and ahead of the twin but is only activated locally at the twin tip boundary and can be driven away from the twin tip within narrow regions oriented at angle from the twin plane.

4. Discussion

4.1. Twin accommodation

In earlier studies, it was shown that the terminating twins such as $\frac{1}{6}\langle 111\rangle\{11\bar{2}\}$ in bcc Mo-35 at.% Re alloys, $\frac{1}{6}\langle 11\bar{2}\rangle\{111\}$ in fcc Co-9.5 wt.% Fe alloys, and $\frac{1}{36}\langle\bar{1}\bar{1}26\rangle\{11\bar{2}1\}$ in hcp Co crystals, are associated with emissary slip structures ahead of them [10–14]. Emissary slip in these crystals occurs to relieve the localized stresses developed in the vicinity of terminating twins [10–14]. In the current study both $\langle a\rangle$ and $\langle c+a\rangle$ glissile dislocations are observed in the vicinity of $(\bar{1}012)$ twins terminating inside the grains of a deformed Mg-0.6 wt.% Y alloy. These dislocations were also found stored along the twin boundary. An interesting observation was a dislocation array connected to the tip of terminating twins. These observations are totally consistent with the emissary slip patterns observed in earlier studies [10–14]. Based on the results described in the preceding sections, a crystallographic relation between $(\bar{1}012)$ twinning shear and the observed matrix glide can be proposed as.

$$15 \times \frac{1}{15}[\bar{1}01\bar{1}]_{(\bar{1}012)} \rightarrow \frac{1}{3}[\bar{2}11\bar{3}]_{(\bar{1}011)} + \frac{1}{3}[\bar{1}\bar{1}20]_{(0001)} \quad (6)$$

As per Frank's rule [29], this decomposition reaction is energetically unfavorable (i.e. $b_{tw}^2 < b_{\langle c+a\rangle}^2 + b_{\langle a\rangle}^2$), however, it could occur to relieve the stresses prevailing in the vicinity of terminating $(\bar{1}012)$ twin from the pile up of twinning partials at the twin tip. According to this reaction, under the influence of appropriate stresses, 15 twinning partials bounding the twin tip may interact and coalesce to generate one pyramidal-I $\langle c+a\rangle$ and one basal $\langle a\rangle$ glissile dislocation. The two product matrix dislocations would then relieve the plastic stresses developed in the vicinity of twin. The high Schmid factor values (section S5 of SM) obtained for these matrix dislocations indicate that they could move and participate in the stress relaxation process. Furthermore, Serra et al. [30], showed that the $\{\bar{1}012\}$ twinning partials have wide-spread core width larger than basal lattice constant ($a = 0.3234\ nm$) and wider than the $\{\bar{1}012\}$ inter-planar spacing (0.1915 nm) of Mg. Therefore, it is possible that the cores of $\{\bar{1}012\}$ twinning partials present on adjacent twin planes could overlap and coalesce to generate matrix glide under the influence of appropriate stress concentrations. In support of this picture of emissary slip, the 3D twin crystal plasticity calculations described in Section 3.5, identified the slip patterns seen in the ex-situ TEM observations as those involved in relaxing the twin tip induced stresses.

In case of cubic metals and alloys the problem of plastic accommodation at terminating twins is relatively simple due to the fact that the slip planes (directions) match with the twinning planes (shear directions) as described in equations (1) and (2). Therefore, it is possible to envisage the exact continuation of twinning shear in these crystals. In contrast to cubic crystals, as described in Eq. (6), neither the twinning plane nor the twinning shear matches with the available slip systems in hcp metals. Consequently, it is difficult to imagine the exact continuation of $\{\bar{1}012\}$ twinning shear to available slip systems in hcp crystals, and it requires a further detailed study. Nevertheless, it should be noted that the $\{\bar{1}012\}$ twinning plane and the glide planes of $\langle a\rangle$ and $\langle c+a\rangle$ slip dislocations share $[\bar{1}2\bar{1}0]$ as a common line of intersection as illustrated by the stereographic projection and schematic in Fig. 7. Based on this observation, it can be speculated that the reaction (6) could occur at the common line of intersection, and the 15 twinning partials may coalesce and propagate the resultant twinning shear in the form of pyramidal-I $\langle c+a\rangle$ and basal $\langle a\rangle$ matrix glide. It is possible that the $\langle c+a\rangle$ dislocations gliding on $(\bar{1}011)$ pyramidal-I plane may cross-slip to other pyramidal planes (i.e., $(\bar{1}101)$ and $(\bar{2}122)$ in this study) and contribute for the contrast parallel to basal plane as shown in Fig. 4.

In earlier studies, Robert et al. [15], using optical microscopy showed that the strain accommodation at $\{\bar{1}012\}$ terminating twins occurs by the formation of kink bands in the Mg matrix. Jonas et al. [16], computed the deformation gradient tensor associated with $\{\bar{1}012\}$ twins and reported that either $\langle c+a\rangle$ slip or mechanical twinning is necessary to accommodate strains in the vicinity of tensile twins in Mg. Based on etch pit analysis, Rosenbaum proposed a reaction between basal and pyramidal dislocations, which could relieve the stresses near $\{\bar{1}012\}$ twin tips in Zn [31]. Although, these studies provide valuable insights on the accommodation of $\{\bar{1}012\}$ twins, the results discussed in the current study showed a direct TEM evidence of emissary $\langle c+a\rangle$ and $\langle a\rangle$ slip near $\{\bar{1}012\}$ twin tips (see Figs. 3 and 4) in Mg-Y alloys.

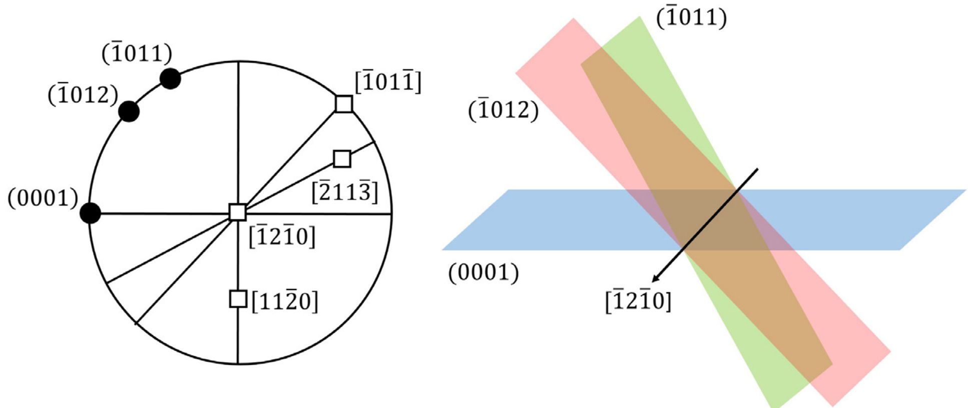

Fig. 7. Standard hcp Mg stereographic projection showing the relation between $(\bar{1}012)$ twinning plane and the glide planes of $\langle a\rangle$ and $\langle c+a\rangle$ dislocations observed in this study. The corresponding Burgers vectors of twinning partials and matrix dislocations are also displayed on the projection. It is clear that the twinning plane and glide planes of matrix dislocations share $[\bar{1}2\bar{1}0]$ as a common line of intersection as illustrated in the schematic.

It should also be noted that emissary slip structures need not always present at terminating twins. Their evolution depend on the twinning shear and thickness of twins, which in turn determine the magnitude of stresses developed in the vicinity of twin tip and microstructure [6,32]. For instance, narrow $\{\bar{1}012\}$ terminating twins in Co are reported to accommodate purely by elastic strain in the surrounding matrix without any plastic deformation [33]. It appears that the thickness of twin described in the current study (Fig. 3) is sufficient to generate high stresses in the surrounding matrix as predicted by the crystal plasticity calculations in Section 3.5, and these stresses are accommodated by $\langle c+a\rangle$ and $\langle a\rangle$ matrix glide as explained by Eq. (6). In order to examine the occurrence of emissary slip at $\{\bar{1}012\}$ terminating twins, we have demonstrated another tensile twin tip of similar thickness, which has stopped propagating inside the grain-3 of deformed alloy. Fig. 8 shows the morphology and structure of this twin. The dislocation contrast analysis identifies an emissary dislocation array (indicated by a black arrow) seen emanating from the tip as a $\langle c+a\rangle$ dislocation array (see section S4 of the SM), which is similar to the situation of the terminating twin described in Figs. 3 and 4.

4.2. Twin nucleation

The nucleation of a twin can be envisaged to occur either homogeneously as postulated by Orowan [34] and Yoo [3] or heterogeneously such as from a suitable defect configuration [6,25,35]. Most of the available defect-assisted twin nucleation models, which have not been verified experimentally, involve the dissociation of $\langle a\rangle$ and $\langle c+a\rangle$ lattice dislocations into numerous glissile twinning partials and a residual imperfect dislocation to conserve the total Burgers vector [6,25,35]. These models basically depend upon the relation between the slip plane (direction) and twinning plane (direction). For instance, Vaidya and Mahajan, using ex-situ TEM proposed a crystallographic relation where the $[1\bar{1}00]$ and $\langle c+a\rangle$ dislocations may interact and dissociate to form a 12-layer $\{11\bar{2}1\}$ twin embryo in hcp Co crystals as per the following equation [14].

$$2\{\frac{1}{3}[\bar{2}113]\}_{(\bar{1}\bar{1}2\bar{1})} + [1\bar{1}00]_{(\bar{1}\bar{1}2\bar{1})} \rightarrow 12 \times \frac{1}{12}\{\frac{1}{3}[\bar{1}\bar{1}26]\}_{(\bar{1}\bar{1}2\bar{1})} \quad (7)$$

Similar crystallographic relations were reported for the nucleation of a 3-layer twin embryo in bcc and fcc crystals. Those are the reactions given in equations (1) and (2), however, in the opposite order [10,11]. The equations (1), (2) and (7) show a relation that the corresponding slip planes and twin planes are the same.

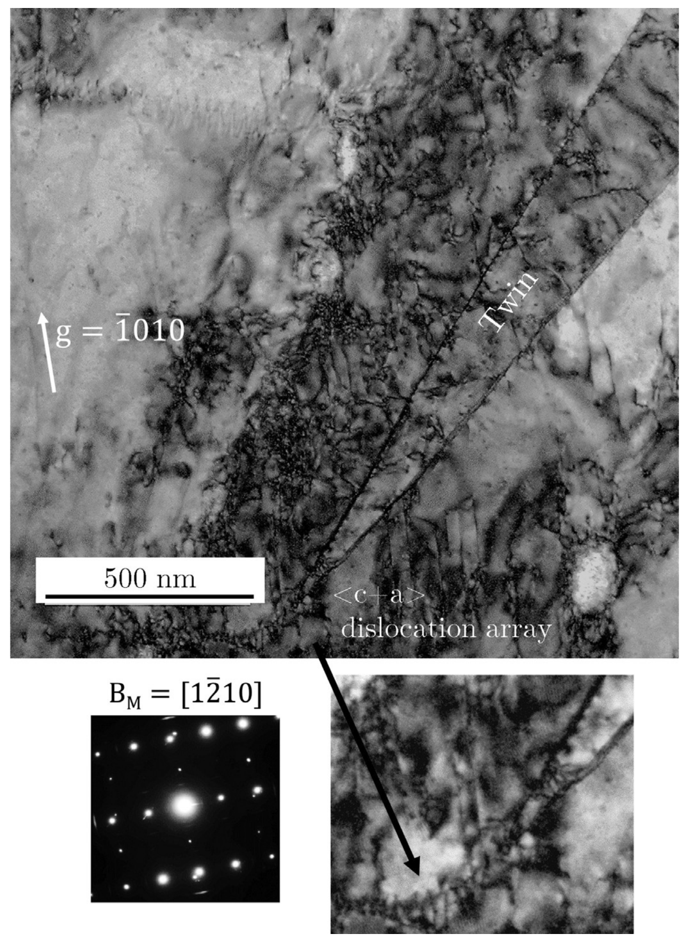

Fig. 8. (a) TEM image of another tensile twin tip which has stopped propagating inside grain-3 of the deformed alloy. The matrix is oriented along the $[1\bar{2}10]$ direction. The experimental SAED pattern shows the spots corresponding to twin as well as the matrix and is consistent with the tensile twinning. The black arrow points a $\langle c+a\rangle$ dislocation array, which is associated with the twin tip, and is similar to the case of twin tip described in Fig. 3.

In the current study based on ex-situ TEM observations, we propose a dislocation reaction where one $\langle c+a\rangle$ and one basal $\langle a\rangle$ matrix dislocation could, under appropriate stress, react to generate a $(\bar{1}012)$ twin embryo consisting of 15 twinning partials as given below

$$\frac{1}{3}[\bar{2}11\bar{3}]_{(\bar{1}011)} + \frac{1}{3}[\bar{1}\bar{1}20]_{(0001)} \rightarrow 15 \times \frac{1}{15}[\bar{1}01\bar{1}]_{(\bar{1}012)}. \quad (8)$$

As discussed in the preceding section the twinning plane and glide planes of matrix dislocations share $[\bar{1}2\bar{1}0]$ as a common line of intersection (see Fig. 7). Therefore, it is possible that the $\langle a \rangle$ and $\langle c+a \rangle$ dislocations could glide and dissociate at the common line of intersection to generate twinning partials on the $(\bar{1}012)$ twin planes. Moreover, as per Frank's rule [29], the dislocation reaction (8) is energetically favorable (i.e. $b^2_{\langle c+a \rangle} + b^2_{\langle a \rangle} > b^2_{tw}$), therefore, it could occur inside the grains under suitable stresses. This reaction suggests that only two matrix dislocations, one $\langle a \rangle$ and one $\langle c+a \rangle$-type are sufficient to generate a twin embryo consisting of 15 twinning partials corresponding to a thickness of 30 crystallographic $\{\bar{1}012\}$ planes. Although, we did not directly observe the 30-layer thick twin embryos in the current study, the correlation between the crystallography of twin and associated dislocation structures (in Fig. 3 and 4) is totally consistent with the dislocation reaction (8). The important implication of this reaction is that *slip precedes* $\{\bar{1}012\}$ *twinning*, which is consistent with the earlier observations of bcc, fcc and hcp metals where slip occurs prior to twinning [10–14].

4.3. Diffraction contrast along twin boundary

The TEM results in this study showed that the diffraction contrast analysis along the twin boundary is consistent with that of lattice dislocations (Fig. 5), suggesting that twin-slip interactions took place during deformation. Various studies have examined twin-slip interactions based on the relationship between the lattice dislocation Burgers vector and the twin-matrix co-zone axis, defined as the direction that contains the twinning plane and glide planes of matrix dislocations (i.e. $[\bar{1}2\bar{1}0]$ in this study, see Fig. 7) [36–42]. For instance, screw dislocations with Burgers vectors parallel to the co-zone axis, can directly cross slip across the twin boundary into the twin domain without leaving any residual defects at the twin boundary [36–42]. In contrast, the dislocations with inclined Burgers vectors to the co-zone axis are absorbed by the twin boundary [36–42]. Chen et al., using molecular dynamics simulations, suggested that the matrix dislocations (basal, prismatic and pyramidal-I) with Burgers vector inclined to the co-zone axis, do not cross slip into the twin, rather they completely absorb by the twin boundary [36]. The Burgers vectors of $\langle a \rangle$ and $\langle c+a \rangle$ slip dislocations obtained in this work, in the vicinity of twins and along the twin boundary, are not parallel to the co-zone axis. Consequently, these dislocations may be absorbed and stored along the twin boundary, resulting in diffraction contrast along the twin boundary for the operating reflections described in Fig. 5. Finally, the diffraction contrast observed along the twin boundary in Fig. 5, is also consistent with that of $(\bar{1}012)$ twinning partials for the first three operating reflections described in Table 1. It is possible that numerous $(\bar{1}012)$ twinning partials can produce contrast along the twin boundary. For instance, a combination of 15 twinning partials can yield $\mathbf{g} \cdot \mathbf{b}_{tw}$ values comparable to that of lattice dislocations (see Table 1). However, it should be noted that the four operating reflections described in Section 3.4, are actually not sufficient to distinguish the contrast originating from the lattice dislocations and twinning partials. Proper choice of reflections is required to distinguish the actual contrast originating from these dislocations.

4.4. Effect of Y on twinning and slip

There are various factors that influence twinning activity in materials, e.g., temperature, strain rate, grain size as well as the orientation, secondary phases, and solute hardening etc[6]. Some of these factors may be strongly interdependent on each other. Stanford et al., studied the effect of high Y content on the twinning behavior of Mg alloys [43]. It has been shown that at low Y concentrations (5 wt.% Y) the $\{\bar{1}012\}$ twins are preferentially activated, whereas high amount of Y (10 wt.% Y) significantly decreases the volume fraction of $\{\bar{1}012\}$ twins [43]. This is due to the fact that the larger atomic size of Y could inhibit the atomic shuffling process required for the formation of $\{\bar{1}012\}$ twins in Mg [43]. It has been also shown that the secondary phases such as precipitates do not directly strongly suppress the *nucleation* of tensile twins in Mg alloys, and their main effect is therefore on the *propagation* and *growth* events [44]. The Mg alloy used in the current study has comparatively low Y concentration (0.6 wt.% Y), therefore, it can be suggested that the hardening due to Y and secondary phases (if any) in the alloy may not strongly effect the nucleation event of tensile twins.

The results in the current study show that the deformation in grain-2 is accommodated by pyramidal-I $\langle c+a \rangle$ slip dislocations having the Burgers vector: $\frac{1}{3}[2\bar{1}\bar{1}3](\bar{1}011)$ and exhibit a Schmid factor value of 0.45 for the orientation of grain-2. No $\langle a \rangle$ slip and tensile twins have been observed in this grain, which may be a consequence of low Schmid factor values (0.38 and 0.33) associated with them in the same order. However, it is not uncommon to notice tensile twins having low Schmid factor values in Mg alloys [16]. We, therefore, speculate that the absence of $\{\bar{1}012\}$ twins in grain-2 may be governed by the prior slip interaction as described in equation (8), which suggests that the formation of $\{\bar{1}012\}$ twin requires a prior interaction between basal $\langle a \rangle$ and pyramidal-I $\langle c+a \rangle$ dislocations. Grain-2 lacked basal $\langle a \rangle$ dislocations making it insufficient to form $\{\bar{1}012\}$ twins.

It has been shown that the alloying element Y enhances the $\langle c+a \rangle$ slip activity and thus, the room temperature ductility of Mg-Y alloys [19]. However, the actual role of Y on the choice of pyramidal-I and pyramidal-II $\langle c+a \rangle$ slip has yet to be clarified and it requires a further study. Sandlobes et al., showed the presence of pyramidal-I as well as pyramidal-II $\langle c+a \rangle$ slip in the deformed Mg-3 wt.% Y alloy [21]. Rikihisa et al., reported that Mg alloys with 0.6-1.1 at% Y yield predominantly by pyramidal-I $\langle c+a \rangle$ slip than pyramidal-II slip, whereas Mg alloys with 1.1-1.3 at% Y are found to yield by prismatic slip [45]. The current study reports $\langle c+a \rangle$ dislocations on pyramidal-I planes and $\langle a \rangle$ dislocations on the basal plane. Moreover, $\langle c+a \rangle$ dislocation contrast parallel to basal planes has been also observed, which is similar to the $\langle c+a \rangle$ dislocation contrast observed in both pure Mg, Mg-3 wt.%Y and Mg-Li alloys [18,21,23,24]. Finally, the zig-zag nature of $\langle c+a \rangle$ dislocations seen in the emissary array (see Fig. 4) may be a result of cross-slip on multiple pyramidal planes as described in Figure S3 of the SM. The observed slip activity along with the tensile twinning in the deformed Mg-0.6 wt.% Y alloy may be an effect of alloying element Y, which in turn provided a favorable situation to study the interrelationship between slip and $\{\bar{1}012\}$ twinning.

5. Conclusions

The accommodation process of plastic stresses developed at $\{\bar{1}012\}$ terminating twins inside the grains of a deformed Mg-0.6 wt.% Y alloy, was investigated ex-situ by TEM and crystal plasticity calculations. Both pyramidal-I $\langle c+a \rangle$ and basal $\langle a \rangle$ dislocations were observed in the vicinity of terminating twins, directly connected to the twin tips, and along the twin boundaries. The observed emissary slip patterns evolve to relax the plastic stresses developed at the tips of $\{\bar{1}012\}$ twins. Based on the results an interrelationship between $\{\bar{1}012\}$ twinning shear and the observed matrix glide has been proposed, which is consistent with the phenomenon of emissary slip. The interrelationship can be expressed as

$$\frac{1}{3}\langle\bar{2}11\bar{3}\rangle_{\{\bar{1}011\}} + \frac{1}{3}\langle\bar{1}\bar{1}20\rangle_{(0001)} \xrightleftharpoons[slip]{twinning} 15\times\frac{1}{15}\langle\bar{1}01\bar{1}\rangle_{\{\bar{1}012\}}$$

where $\mathbf{b}_{tw} = \frac{1}{15}\langle\bar{1}01\bar{1}\rangle$ is the Burgers vector of twinning partials for $\{\bar{1}012\}$ twins in Mg. The proposed interrelationship, under appropriate stresses, could elucidate the generation of numerous twinning partials needed for the development of a stable $\{\bar{1}012\}$ twin embryo, as well as the accommodation process of stresses developed in the vicinity of twins terminating inside the grains of Mg-Y alloy.

Declaration of Competing Interest

The authors declare that they have no known competing financial interests or personal relationships that could have appeared to influence the work reported in this paper.

Acknowledgments

The authors acknowledge the financial support from the National Science Foundation NSF CMMI-1723539, NSF CMMI-1729887, and NSF CMMI-1729829. BL would like to acknowledge financial support from the Department of Defense (DoD) through the National Defense Science & Engineering Graduate (NDSEG) Fellowship Program and Los Alamos National Laboratory (LANL) Institute of Materials Science (IMS) funding. MAK acknowledges the financial support from the US Department of Energy, Office of Basic Sciences Project FWP 06SCPE401.

Supplementary material

Supplementary material associated with this article can be found, in the online version, at 10.1016/j.actamat.2020.116514

References

[1] M. Easton, A. Beer, M. Barnett, C. Davies, G. Dunlop, Y. Durandet, S. Blacket, T. Hilditch, P. Beggs, Magnesium alloy applications in automotive structures, JOM 60 (2008) 57–62, doi:10.1007/s11837-008-0150-8.
[2] M. Hakamada, T. Furuta, Y. Chino, Y. Chen, H. Kusuda, M. Mabuchi, Life cycle inventory study on magnesium alloy substitution in vehicles, Energy 32 (2007) 1352–1360, doi:10.1016/j.energy.2006.10.020.
[3] M.H. Yoo, J.K. Lee, Deformation twinning in HCP metals and alloys, Phil. Mag. A 63 (1991) 987–1000, doi:10.1080/01418619108213931.
[4] H.E. Kadiri, C.D. Barrett, J. Wang, C.N. Tome, Why are $\{\bar{1}012\}$ twins profuse in magnesium, Acta Mater. 85 (2015) 354–361, doi:10.1016/j.actamat.2014.11.033.
[5] M.R. Barnett, Twinning and the ductility of magnesium alloys: Part I: "Tension" twins, Mater. Sci. Eng. A 464 (2007) 1–7, doi:10.1016/j.msea.2006.12.037.
[6] J.W. Christian, S. Mahajan, Deformation twinning, Prog. Mater. Sci. 39 (1995) 1–157, doi:10.1016/0079-6425(94)00007-7.
[7] M.R. Barnett, N. Stanford, A. Ghaderi, F. Siska, Plastic relaxation of the internal stress induced by twinning, Acta Mater. 61 (2013) 7859–7867, doi:10.1016/j.actamat.2013.09.024.
[8] M.R. Barnett, Twinning and the ductility of magnesium alloys: Part II: "Contraction" twins, Mater. Sci. Eng. A 464 (2007) 8–16, doi:10.1016/j.msea.2007.02.109.
[9] D. Ando, J. Koike, Y. Sutou, The role of deformation twinning in the fracture behaviour and mechanism of basal texture magnesium alloys, Mater. Sci. Eng. A 600 (2014) 145–152, doi:10.1016/j.msea.2014.02.010.
[10] S. Mahajan, Interrelationship between slip and twinning in BCC crystals, Acta Metall. 23 (1975) 671–684, doi:10.1016/0001-6160(75)90049-8.
[11] S. Mahajan, C.Y. Chin, Formation of deformation twins in FCC crystals, Acta Metall. 21 (1973) 1353–1363, doi:10.1016/0001-6160(73)90085-0.
[12] S. Mahajan, Evaluation of slip patterns observed in association with deformation twins in Mo-35 at% Re alloy, J. Phys. F. Metal. Phys. 2 (1972) 19–23, doi:10.1088/0305-4608/2/1/006.
[13] A.W. Sleeswyk, Twinning and the origin of cleavage nuclei in $\alpha-$iron, Acta Metall. 10 (1962) 803–812, doi:10.1016/0001-6160(62)90094-9.
[14] S. Vaidya, S. Mahajan, Accommodation and formation of $\{11\bar{2}1\}$ twins in Co single crystals, Acta Metall. 28 (1980) 1121–1131, doi:10.1016/0001-6160(80)90095-4.
[15] E. Roberts, P.G. Partridge, The accommodation around $\{\bar{1}012\} < 10\bar{1}1 >$ twins in magnesium, Acta Metall. 14 (1966) 513–527, doi:10.1016/0001-6160(66)90319-1.
[16] J.J. Jonas, S. Mu, T. Al-Samman, G. Gottstein, L. Jiang, E. Martin, The role of strain accommodation during the variant selection of primary twins in magnesium, Acta Mater. 59 (2011) 2046–2056, doi:10.1016/j.actamat.2010.12.005.
[17] A. Khosravani, D.T. Fullwood, B.L. Adams, T.M. Rampton, M.P. Miles, R.K. Mishra, Nucleation and propagation of $\{10\bar{1}2\}$ twins in AZ31 magnesium alloy, Acta Mater. 100 (2015) 202–214, doi:10.1016/j.actamat.2015.08.024.
[18] S.R. Agnew, J.A. Horton, M.H. Yoo, Transmission electron microscopy investigation of $< c + a >$ dislocations in Mg and $\alpha-$solid solution Mg-Li alloys, Metall. Mater. Trans. A 33 (2002) 851–858, doi:10.1007/s11661-002-0154-x.
[19] S. Sandlobes, M. Friak, S. Zaefferer, A. Dick, S. Yi, D. Letzig, Z. Pei, L.F. Zhu, J. Neugebauer, D. Raabe, The relation between ductility and stacking fault energies in Mg and Mg-Y alloys, Acta Mater. 60 (2012) 3011–3021, doi:10.1016/j.actamat.2012.02.006.
[20] S. Sandlobes, S. Zaefferer, I. Schestakow, S. Yi, R. Gonzalez-Martinez, On the role of non-basal deformation mechanisms for the ductility of Mg and Mg-Y alloys, Acta Mater. 59 (2011) 429–439, doi:10.1016/j.actamat.2010.08.031.
[21] S. Sandlobes, M. Friak, J. Neugebauer, D. Raabe, Basal and non-basal dislocation slip in Mg-Y, Mater. Sci. Eng. A 576 (2013) 61–68, doi:10.1016/j.msea.2013.03.006.
[22] M. Niewczas, Lattice correspondence during twinning in hexagonal close packed crystals, Acta Mater. 58 (2010) 5848–5857, doi:10.1016/j.actamat.2010.06.059.
[23] T. Obara, H. Yoshinga, S. Morozumi, $\{11\bar{2}2\}\langle\bar{1}\bar{1}23\rangle$slip system in magnesium, Acta Metall. 21 (1973) 845–853, doi:10.1016/0001-6160(73)90141-7.
[24] B. Li, Q.W. Zhang, S.N. Mathaudhu, Basal-pyramidal dislocation lock in deformed magnesium, Scripta Mater. 134 (2017) 37–41, doi:10.1016/j.scriptamat.2017.02.040.
[25] N. Thompson, D.J. Millard, Xxxviii. twin formation, in cadmium, Phil. Mag. 43 (1952) 422–440, doi:10.1080/14786440408520175.
[26] M. Kumar, A. Kanjarla, S. Niezgoda, R. Lebensohn, C. Tome, Numerical study of the stress state of a deformation twin in magnesium, Acta Mater. 84 (2015) 349–358, doi:10.1016/j.actamat.2014.10.048.
[27] M. Kumar, I.J. Beyerlein, C. Tome, Effect of local stress fields on twin characteristics in HCP metals, Acta Mater. 116 (2016) 143–154, doi:10.1016/j.actamat.2016.06.042.
[28] J. Wang, X. Wang, K. Yu, T.J. Rupert, S. Mahajan, E.J. Lavernia, J.M. Schoenung, I.J. Beyerlein, Manipulating deformation mechanisms with Y alloying of Mg, Mater. Sci. Eng. A (2020) Inreview.
[29] F.C. Frank, On the equation of motion of crystal dislocations, Proc. Phys. Soc. A 62 (1949) 131, doi:10.1088/0370-1298/62/2/307.
[30] A. Serra, D.J. Bacon, Computer simulation of twinning dislocation in magnesium, Phil. Mag. 63 (1991) 1001–1012, doi:10.1080/01418619108213932.
[31] H.R. Rosenbaum, Non-basal slip and twin accommodation in zinc crystals, Acta Metall. 9 (1961) 742, doi:10.1016/0001-6160(61)90104-3.
[32] M.L. Green, M. Cohen, Pseudotwinning and pseudoelasticity in βFe-Be alloys, Acta Metall. 27 (1979) 1523, doi:10.1016/0001-6160(79)90175-5.
[33] S. Vaidya, S. Mahajan, Glide ahead of terminating $\{10\bar{1}2\}$ twins in Co, Scripta Metall. 14 (1980) 623, doi:10.1016/0036-9748(80)90010-1.
[34] E. Orowan, Dislocations in metals (Ed. M. Cohen), New York, NY: The Institute of Metals Division, The Americal Institute of Mining and Metallurgical Engineers, Inc. (1954) 69–195.
[35] S. Mendelson, Dislocation dissociations in HCP metals, J. Appl. Phys. 41 (1970) 1893–1910, doi:10.1063/1.1659139.
[36] P. Chen, F. Wang, B. Li, Dislocation absorption and transmutation at $\{10\bar{1}2\}$ twin boundaries in deformation of magnesium, Acta Mater. 164 (2019) 440–453, doi:10.1016/j.actamat.2018.10.064.
[37] F. Wang, C.D. Barrett, R.J. McCabe, H.E. Kadiri, L. Capolungo, S.R. Agnew, Dislocation induced twin growth and formation of basal stacking faults in $\{10\bar{1}2\}$ twins in pure Mg, Acta Mater. 165 (2019) 471–485, doi:10.1016/j.actamat.2018.12.003.
[38] J. Zhang, G. Xi, X. Wan, C. Fang, The dislocation-twin interaction and evolution of twin boundary in AZ31 Mg alloy, Acta Mater. 133 (2017) 208–216, doi:10.1016/j.actamat.2017.05.034.
[39] M.H. Yoo, C.T. Wei, Growth of deformation twins in zinc crystals, Phil. Mag. 14 (1966) 573–587, doi:10.1080/14786436608211952.
[40] A. Serra, D.J. Bacon, A new model for $\{10\bar{1}2\}$ twin growth in HCP metals, Phil. Mag. 73 (1996) 333–343, doi:10.1080/01418619608244386.
[41] D.I. Tomsett, D.I.M. Bevis, The incorporation of basal slip dislocations in $\{\bar{1}012\}$ twins in zinc crystals, Phil. Mag. 19 (1968) 129–140, doi:10.1080/14786436908217768.
[42] M. Gong, G. Liu, J. Wang, L. Capolungo, C.N. Tome, Atomistic simulations of interaction between basal $< a >$ dislocations and three-dimensional magnesium, Acta Mater. 155 (2018) 187–198, doi:10.1016/j.actamat.2018.05.066.
[43] N. Stanford, R.K.W. Marceau, M.R. Barnett, The effect of high yttrium solute concentration on the twinning behaviour of magnesium alloys, Acta Mater. 82 (2015) 447–456, doi:10.1016/j.actamat.2014.09.022.
[44] J.D. Robson, M.R. Barnett, The effect of precipitates on twinning in magnesium alloys, Adv. Eng. Mater. 21 (2019) 1800460, doi:10.1002/adem.201800460.
[45] H. Rikihisa, T. Mori, M. Tsushida, H. Kitahara, S. Ando, Influence of yttrium addition on plastic deformation of magnesium, Mater. Trans. 58 (2017) 1656–1663, doi:10.2320/matertrans.M2017265.